FRONTIERS OF PHYSICS

RESEARCH ARTICLE
Volume 18 / Issue 5 / 53305 / 2023

Room-temperature vertical ferroelectricity in rhenium diselenide induced by interlayer sliding

Fang Li[1], Jun Fu[2], Mingzhu Xue[3], You Li[1], Hualing Zeng[2], Erjun Kan[1], Ting Hu[1,†], Yi Wan[1,3,‡]

1 MIIT Key Laboratory of Semiconductor Microstructure and Quantum Sensing, and Department of Applied Physics, Nanjing University of Science and Technology, Nanjing 210094, China
2 International Center for Quantum Design of Functional Materials (ICQD), Hefei National Laboratory for Physical Sciences at the Microscale, and Department of Physics, University of Science and Technology of China, Hefei 230026, China
3 State Key Laboratory for Artificial Microstructure & Mesoscopic Physics, School of Physics, Peking University, Beijing 100871, China
Corresponding authors. E-mail: †thu@njust.edu.cn, ‡wany@njust.edu.cn
Received March 30, 2023; accepted May 4, 2023

ABSTRACT

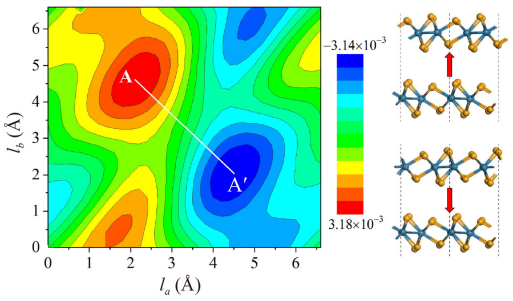

One variety of ferroelectricity that results from lateral relative movements between the adjacent atomic layers is referred to as sliding ferroelectricity, which generates an interfacial charge transfer and hence a polarization reversal. The mechanism of sliding ferroelectricity existent in van der Waals crystals is quite distinct from the conventional ferroelectric switching mechanisms mediated by ion displacement. It creates new possibilities for the design of two-dimensional (2D) ferroelectrics since it can be achieved even in non-polar systems. Before 2D ferroelectrics can be widely employed for practical implementations, however, there is still significant work to be done on several fronts, such as exploring ferroelectricity possibly in more potential 2D systems. Here, we report the experimental observation of room-temperature robust vertical ferroelectricity in layered semiconducting rhenium diselenide ($ReSe_2$), a representative member of the transition metal dichalcogenides material family, based on a combined research of nanoscale piezoresponse and second harmonic generation measurements. While no such ferroelectric behavior was seen in 1L $ReSe_2$, 2L $ReSe_2$ exhibits vertical ferroelectricity at ambient environment. Based on density-functional theory calculations, we deduce that the microscopic origin of ferroelectricity for $ReSe_2$ is uncompensated vertical charge transfer that is dependent on in-plane translation and switchable upon interlayer sliding. Our findings have important ramifications for the ongoing development of sliding ferroelectricity since the semiconducting properties and low switching barrier of $ReSe_2$ open up the fascinating potential for functional nanoelectronics applications.

Keywords rhenium diselenide, transition metal dichalcogenides, vertical ferroelectricity, sliding ferroelectricity

1 Introduction

Ferroelectric materials are a type of functional material that, within a certain temperature range, exhibits spontaneous electric polarization even in the absence of an external electric field [1, 2]. Spontaneous polarization is the fundamental building block for a wide range of technological applications, such as ferroelectric field-effect transistors, non-volatile memory devices, and active elements in electro-mechanical and electro-optical systems. In response to the introduction of an external electric field that breaks the degeneracy, it can be

Higher Education Press

https://doi.org/10.1007/s11467-023-1304-4

repeatedly switched between two or more energetically equivalent states. The ability to alter electric polarization is a critical component of contemporary nanotechnology. Nowadays, the study of ferroelectric properties at the nanoscale has emerged as a hot topic in the research field of novel functional materials [3, 4], in line with the rapid development of micro-nano technology and the tendency toward miniaturization, integration, and multi-functionalization of electronic components. One of the objectives being pursued by researchers is to figure out how to incorporate ferroelectricity in 2D materials, and ultimately to fabricate multi-state and multi-functional nanoelectronic devices. Through theoretical and experimental investigations, scientists have made significant advancements in recent years. In these experimentally demonstrated 2D ferroelectric materials, such as $CuInP_2S_6$ [5–7] and α-In_2Se_3 [8–10], the spontaneous polarization generates as a result of the relative displacement of atoms, which is strictly constrained by lattice symmetry and structural stability. Until now, only a few 2D layered materials have had their intrinsic ferroelectricity experimentally verified.

To expand the family of 2D ferroelectrics, researchers have proposed that interlayer sliding can generate ferroelectricity in bilayer or few-layer van der Waals materials via the utilization of the unique layer degrees of freedom. A large number of 2D layered materials can exhibit the special feature of "sliding ferroelectricity" [11, 12], even though their bulk-phase structure is not polarized. Experimental evidence for interlayer sliding-induced 2D ferroelectricity has been reported in metallic WTe_2 [13–15], AB-stacked *h*BN bilayers [16–19], InSe [20, 21], transition metal dichalcogenides (TMDs) bilayers [22, 23], and an amphidynamic single crystal (15-crown-5) Cd_3Cl_6 [24]. These ground-breaking scientific developments have made it possible to design and manufacture 2D ferroelectrics from non-polar materials, and have also given rise to a brand-new area of research called slidetronics. 2D semiconducting materials with modest bandgaps are preferred for further slidetronics research. The materials are more promising due to their semiconducting characteristics such as efficient gate tunability and capacity in direct integration into optoelectronics. In contrast, it is challenging to implement these advantages in a metallic or insulating system. Itinerant electrons, for instance, may shield the spontaneous vertical polarization of multilayer WTe_2 due to its metallic characteristics, reducing its significance in practical applications. In this sense, the search for sliding ferroelectricity in semiconductors not only benefits the investigation of performance modulation strategies but also facilitates potential technological applications.

Here, we report the experimental evidence of robust vertical ferroelectricity in $ReSe_2$, a semiconducting counterpart of isostructural semimetal TMDs such as $MoTe_2$ and WTe_2, based on a combined study of micro-zone scanning probe microscopy techniques and non-linear optical effects. In contrast to 1L $ReSe_2$, which shows no discernible ferroelectric signal, 2L $ReSe_2$ exhibits vertical ferroelectricity in an ambient environment. Our density-functional theory (DFT) calculations further demonstrate that the out-of-plane polarization of $ReSe_2$ may be switched through an interlayer shear motion, in stark contrast to the conventional ferroelectric switching mechanism mediated by ion displacement. The semiconducting characteristics and low switching barrier of $ReSe_2$ make it an alluring candidate for use in functional nanoelectronics.

2 Experimental section

Sample preparation. Using the elements in the proper stoichiometric ratios and I_2 as the transport agent, high-quality single crystals of $ReSe_2$ were prepared through a chemical transport reaction. Solid-state precursors were packed together in a quartz ampule (10 mm outer diameter, 200 mm length). The ampule was evacuated to a pressure of around 10^{-4} torr, sealed, and then placed in a two-zone furnace with the source and growth zones set at 1060 and 1000°C, respectively.

Property characterization. TEM (Tecnai F30, FEI), XRD (X' Pert Pro, PANalytical B.V.), and XPS (PHI Quantera II, Ulvac-Phi) were used to analyze the elemental composition and crystalline structure of $ReSe_2$. Optical microscopy (Axio Imager A2m, Zeiss) and AFM (Asylum Research, Cypher S) were used to determine the sample thickness. Based on a commercial confocal optical system (Alfa300R, WITec) equipped with 2.33 eV (532 nm) and 1.96 eV (633 nm) lasers and dispersed by a spectrometer supplied with a diffraction grating of 1800 grooves/mm, Raman spectra of $ReSe_2$ were acquired. The excitation beam was focused onto the sample surface, and the scattering lights were concurrently collected using a 100× objective lens.

PFM measurement. The AFM system with the PFM module was used to probe piezoresponse signals from $ReSe_2$. The rectangular-shaped ASYELEC.01-R2 conductive tips utilized in our PFM experiments have an Ir/Ti (20/5 nm) coating, a spring of 2.8 N/m, and a basis resonant frequency of about 90 kHz. By delivering an AC signal of 200–800 mV beneath the tip-sample contact third-order resonant frequency (270 kHz) and superimposing it on a series of DC triangle saw-tooth waveform voltages (0.1–0.2 Hz), the local switching spectroscopic hysteresis loops were monitored in the resonance-enhanced PFM mode.

SHG measurement. To produce ultrafast light of femtosecond magnitude, a Ti-sapphire lock-in laser is employed as the excitation source with optical pulses of about 800 nm and a repetition frequency of 76 MHz. An optical parameter oscillator (OPO) may then generate

lasers with tunable wavelengths between 500 and 1600 nm, which can subsequently be converted to polarized light using a polarizer and a half-wave plate. The light is focused onto the sample by the objective lenses (100 ×, N.A. = 0.95), with a spot size of around 2.0 μm. The same lenses are then used to gather the SHG signals produced by the non-centrosymmetric sample, and a dichroic beam splitter is used to separate them. The excitation components are filtered by placing a short-wave pass filter in front of the spectrometer.

3 Calculational section

Our first-principles calculations based on the DFT were conducted by VASP, where the PAW method and the PBE exchange-correlation potential function were performed. The optimization of the geometry structure was employed by the conjugated gradient minimization scheme with full-relaxed atomic positions and crystal lattice constants. The convergence criteria for ionic and electronic relaxations were set to be 0.001 eV/Å and 10^{-5} eV/atom, respectively. And, the vacuum space was set to be above 20 Å, large enough to prevent interlayer interactions. In the 2D Brillouin integration, a 10 × 10 × 1 Monkhorst-Pack grid was involved. The weak long-range vdWs interactions were semi-empirically described by the DFT-D3 method. The electric polarization was calculated by the evaluation of the Berry phase expressions of polarization in modern theory.

4 Results and discussion

Similar to other TMDs, $ReSe_2$ crystals are layered materials composed of covalently bound monolayers stacked vertically by van der Waals interactions. Three atomic planes (Se–Re–Se) make up each $ReSe_2$ monolayer. Nevertheless, $ReSe_2$ does not crystallize in the normal 2H or 1T phases found in other TMDs materials such as MoS_2 and $MoTe_2$. Instead, it does so in a unique deformed triclinic 1T′ structure belonging to the low symmetry space group of $P_{\bar{1}}$. As schematically depicted in the crystal structure [Fig. 1(a)], the formation of the in-plane Re_4 "diamond" chains is considered a distortion of Re atoms from their ideal octahedral sites. The unique behavior of Re atoms caused by the $5d^3$ electronic configuration results in a weaker interlayer coupling than other TMDs and a striking in-plane anisotropy.

In our experiments, 1T′-phase $ReSe_2$ bulk crystals were prepared in large quantities using a chemical vapor transport (CVT) method, as seen in the inset of Fig. 1(b) and Fig. S1 of the Electronic Supplemental Material (ESM). X-ray diffraction (XRD) technique was employed to examine the crystal structures of the bulk samples of CVT method-prepared $ReSe_2$ samples. Figure 1(b) indicates that the reflection peaks at 13.9°, 28.0°, 42.5°, and 57.7°, which correspond to the lattice planes of (001), (002), (003), and (004) for $ReSe_2$, revealing the nature of the triclinic 1T′ phase (JCPDS Nos. 50-0537, 82-1379 and 89-0340) [25, 26]. The preferred orientation effect existent in the growth process of the layered $ReSe_2$ crystal is indicated by the (001) peak's strongest intensity. The higher crystallization quality is indicated by the modest full width at half maximum for the (001) plane of around 0.099° (Fig. S2 of the ESM). Moreover, X-ray photoelectron spectroscopy (XPS) was used to examine the elementary composition and bonding configuration of the prepared $ReSe_2$. The high-resolution XPS spectrum for Re 4*f* states as plotted in the left panel of Fig. 1(c) was used to study the bonding states of Re. Two characteristic peaks can be seen at energies of 40.3 eV and 39.3 eV, respectively, which correspond to the core $4f^{5/2}$ and $4f^{7/2}$ level peaks of Re^{4+}. Two distinguishing peaks for the bonding states of Se are found at 53.3 eV and 52.3 eV, respectively, and correspond to the core $3d^{3/2}$ and $3d^{5/2}$ level peaks of Se^{2-}, as depicted in the right panel of Fig. 1(c). The reported statistics for $ReSe_2$ [27, 28] are consistent with our measured XPS results. Moreover, the stoichiometric value of ideal $ReSe_2$ is 1:2, which matches the Re and Se ratio obtained by the XPS results.

To examine the crystal structure of the CVT method-prepared samples, we thinned $ReSe_2$ by mechanical exfoliation [Fig. 2(a)] and transferred it onto a carbon membrane-coated copper microgrid [Fig. 2(b)]. As already mentioned, in contrast to the 1T phase, the 1T′ phase displays covalent bonding between metal atoms (here Re). Re atoms that are covalently connected to one another arrange to form chains that resemble diamonds. More often than not, $ReSe_2$ crystals cleave along these chains. As seen in the optical microscope observation results in Fig. 2(a), the Re chains are currently discovered to correlate with one of the cleaved edges of the few-layer $ReSe_2$ films, providing a first clue of the crystal orientation. Figure 2(c) presents the captured atomically resolved, high-resolution TEM image of the few-layered $ReSe_2$ flakes. The formation of the one-dimensional rhenium "diamond" chains was well suited to the 1T′ structure. It was discovered that the orientations of $\boldsymbol{a}$[100] and $\boldsymbol{b}$[010] were 120° apart. Additionally, we captured selected area electron diffraction (SAED) patterns from the $ReSe_2$ flakes, along with the well-ordered diffraction spots revealing that the prepared $ReSe_2$ is single-crystalline [Fig. 2(d)]. We subsequently investigated the structural anisotropy of the prepared $ReSe_2$ flakes using angle-resolved polarized Raman spectroscopy, a powerful technique for empirically determining the crystal orientations of anisotropic materials. In order to gather the polarization-dependent Raman spectra on $ReSe_2$ thin flakes, we used 532 nm and 633 nm linearly polarized lasers. The measured $ReSe_2$ sample region has been marked by a red cross-

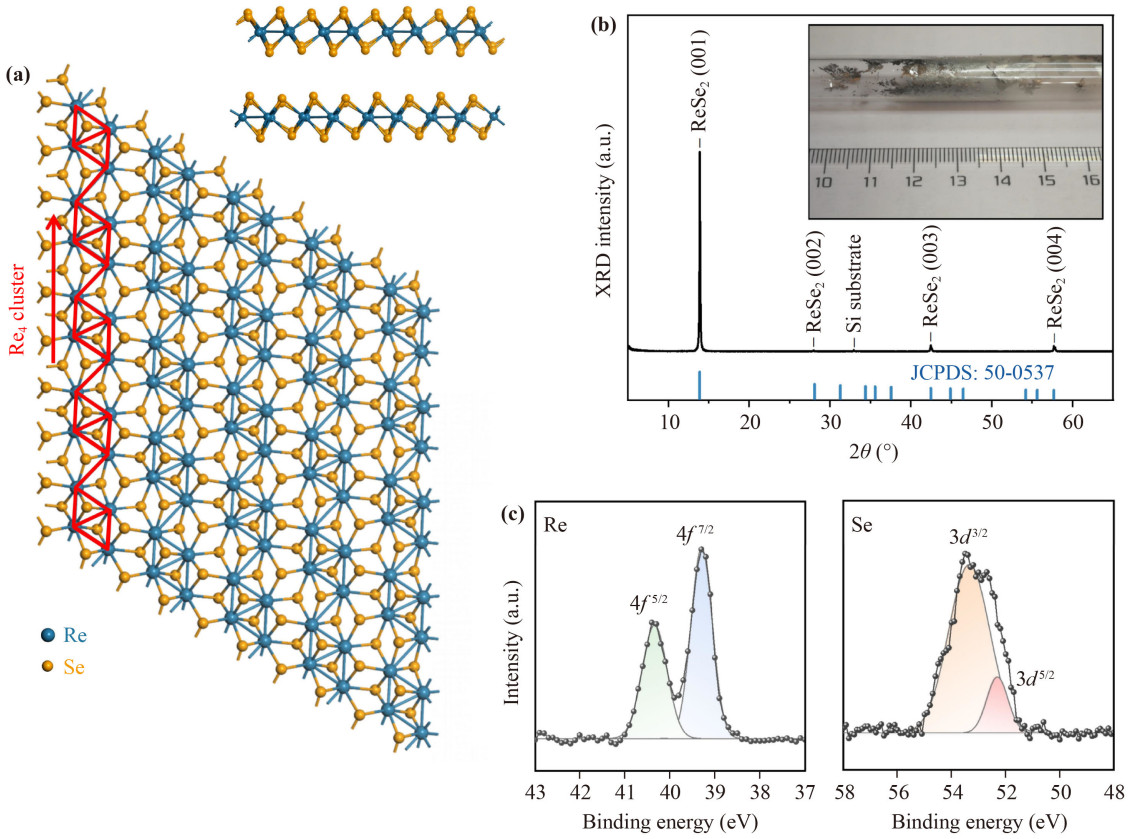

Fig. 1 **(a)** Top and side views of 1T′-$ReSe_2$, where the "diamond" chains of Re_4 clusters have been highlighted in red. **(b)** XRD pattern of the prepared $ReSe_2$ sample and the standard card of triclinic $ReSe_2$ (JCPDS No. 50-0537). Inset: The $ReSe_2$ bulk-form crystals prepared by the CVT method in the sealed ampoule. **(c)** High-resolution XPS spectra collected from the prepared $ReSe_2$ sample.

shaped star shown in Fig. 2(a). Figures 2(e) and (f) display the evolution of Raman spectra obtained by the excitation wavelengths of 532 nm and 633 nm, respectively, for $ReSe_2$, recorded as a function of the angle between the linearly polarized excitation laser and the Re chains in the parallel configuration. The unpolarized Raman spectra of $ReSe_2$ and the polar coordinate representation for polarization-dependent Raman spectra are provided in Fig. S3 of the ESM. The Raman characteristic peaks of $ReSe_2$ display a clear variation of intensity with the angle for all modes, which are clear indications of in-plane anisotropy [29].

Atomic force microscopy (AFM) presents a workable approach to directly study the surface morphology and to precisely estimate the sample terrace height. In addition, optical contrast provides a more useful, non-destructive method to calculate the number of layers. Both two approaches provide strong support for further characterization of 1L, 2L, and few-layer $ReSe_2$ samples. The ultrathin $ReSe_2$ samples were transferred onto a flexible polydimethylsiloxane (PDMS) substrate using mechanical exfoliation. We initially identified the ultrathin regions of the target $ReSe_2$ sample with an optical microscope and captured an image of it [Fig. 3(a)]. The normalized optical contrast (green channel gray value) along the red dotted line depicted in the green channel (G) image was then plotted using the *ImageJ* software after the G image [inset, Fig. 3(b)] was acquired. These variables make it simple to calculate the layer thickness and enable us to look up ultrathin $ReSe_2$ sample region on a transparent substrate. According to the data, the optical contrasts at the highlighted sites, which correspond to 1L, 2L, and 4L $ReSe_2$, are 5.1%, 12.5%, and 33.3%, respectively. Previous reports on sister materials of $ReSe_2$, including grapheme [30], MoS_2 [31], and ReS_2 [32], have all demonstrated the accuracy of this technique for thickness identification. The method can be easily implemented using only an optical microscope.

A ferroelectric material, by definition, should possess switchable spontaneous polarization. It is feasible to demonstrate that ultrathin samples contain switchable ferroelectric polarization using piezoresponse force microscopy (PFM) [5, 8, 15, 23]. PFM tests need to be performed on conductive substrates. However, the optical contrast of $ReSe_2$ atop conducting substrates is relatively poor. Therefore, we would like to obtain $ReSe_2$ fewlayers by mechanical exfoliation from the bulk crystal and transfer them onto PDMS. $ReSe_2$ samples will exhibit

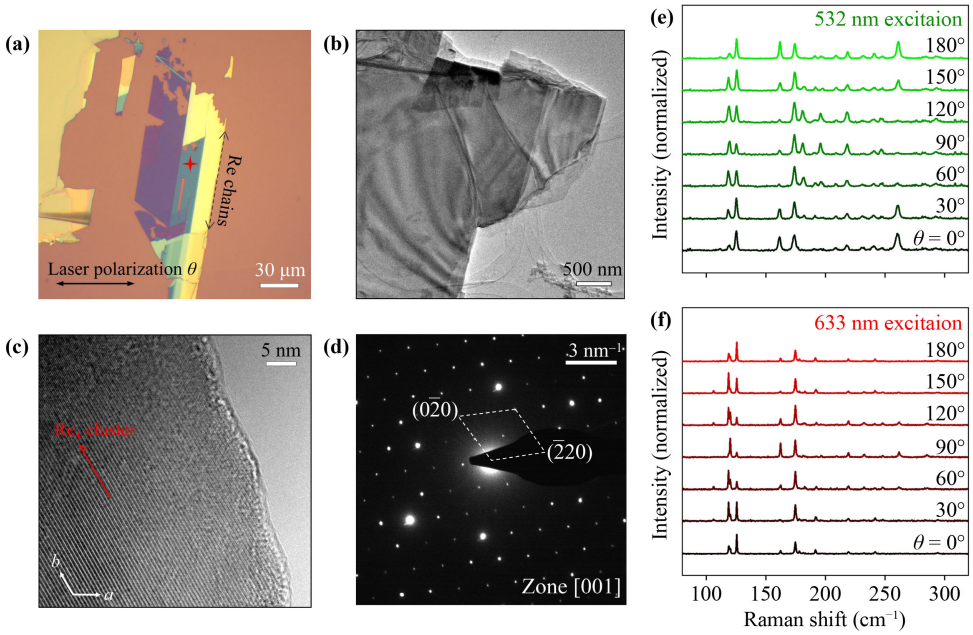

Fig. 2 **(a)** Optical microscopy image of a mechanically exfoliated $ReSe_2$ supported atop SiO_2/Si wafer. **(b, c)** TEM images of $ReSe_2$. **(d)** SAED patterns of $ReSe_2$. **(e, f)** A series of Raman spectra obtained from a $ReSe_2$ sample, recorded as a function of the angle between the linearly polarized excitation and the Re chains at the excitation wavelength of 532 nm (e) and 633 nm (f) under the parallel configuration. The raw spectra are collected from a few-layer $ReSe_2$ region as marked by a red cross-shaped star in (a) and vertically offset for clarity.

thickness-dependent intensities of reflected light on transparent PDMS substrate. We can then conveniently look up ultrathin $ReSe_2$ samples under an optical microscope. By optical contrast analysis, we can find a relatively thin sample region, mark the location, and then transfer the targeted sample region from PDMS onto the conducting substrate via a three-axis micromanipulator, which saves time compared with the search for $ReSe_2$ samples on conducting substrates with poor visibility. The conducting substrates used our experiments for the thinned $ReSe_2$ nanoflakes with 1L (0.76 nm, region I) and 2L (1.70 nm, region II) areas was the SiO_2/Si wafer covered in a Pt (90 nm)/Ni (10 nm) coating [Figs. 4(a) and (b)].

To demonstrate whether the ferroelectric polarization exists in $ReSe_2$, spectroscopic PFM studies were conducted. The piezoresponse signal from 2L $ReSe_2$ exhibits switchable hysteretic behavior as a function of applied bias, similar to conventional ferroelectric materials [bottom panels, Figs. 4(c) and (d)]. The PFM amplitude signal displays a distinctive "butterfly" shape, and the PFM phase signal exhibits a characteristic phase inversion (i.e., a phase value change of around 180°) at the amplitude response minima. Nevertheless, 1L $ReSe_2$ displays very little phase or amplitude contrast, as evidenced in the spectroscopic PFM loops randomly recorded from the

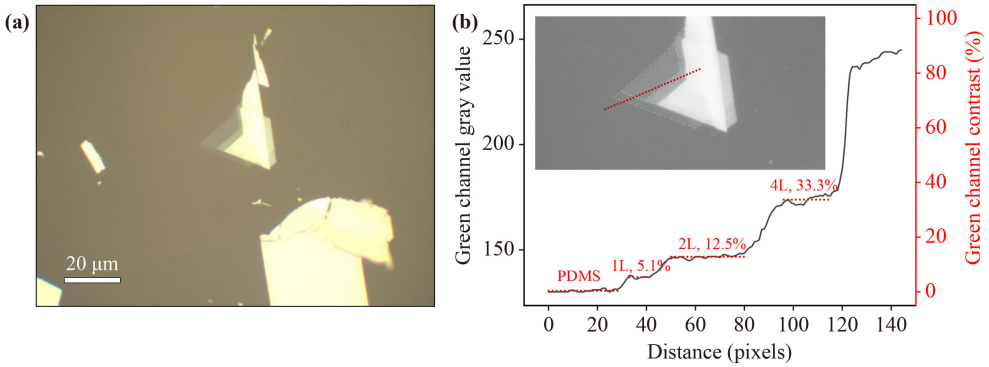

Fig. 3 **(a)** Optical microscopy image of the ultrathin $ReSe_2$ samples with 1L and 2L regions on PDMS. **(b)** Contrast distribution and gray value of the red dotted line shown in the inset of (b). Inset: The green channel image of (a) obtained by the *ImageJ* software.

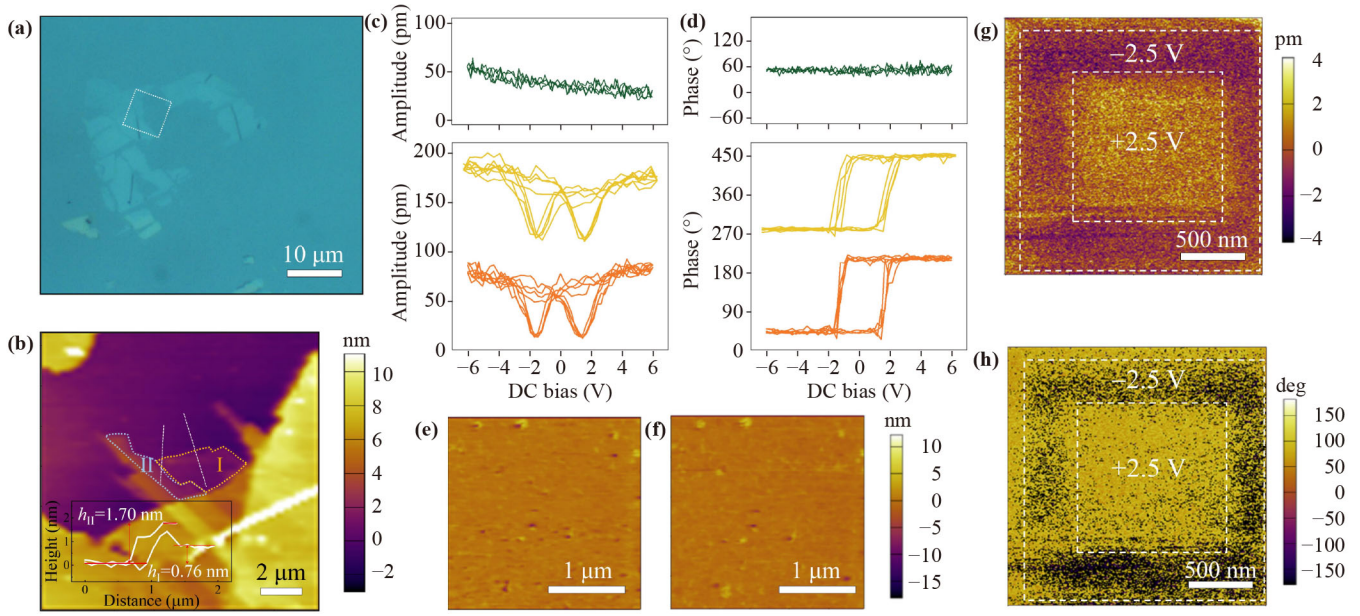

Fig. 4 **(a)** Optical microscopy image of a $ReSe_2$ flake, transferred onto Pt/Ni/SiO_2/Si substrate. **(b)** AFM image for the region denoted by a white dashed square in (a). **(c, d)** Butterfly-shaped amplitude-voltage loops (c) and phase-voltage hysteretic curves (d) for 1L (region I) and 2L (region II) $ReSe_2$, obtained by the switching spectroscopic PFM technique. **(e, f)** AFM images of the areas before (e) and after (f) ferroelectric switching. No obvious morphology damage occurred. **(g)** PFM amplitude image for a 2L $ReSe_2$ with a written box-in-box pattern obtained under reverse DC voltages. **(h)** PFM phase image corresponding to (g).

monolayer region of this material [top panels, Figs. 4(c) and (d)], proving the lack of switchable polarization. We used switching bias pulses with the following capture of PFM pictures to record the residual state in order to directly observe these switchable polarization states. The residual polarization that has been bias-driven and oppositely oriented is apparent clearly in the PFM images of different color contrasts [Figs. 4(g) and (h)]. The initially nearly uniform contrasts of both the PFM amplitude and phase images are inverted by a negative DC bias and result in opposite phase contrast. By inverting the polarity of the applied writing bias, this bias-induced crossover between anti-parallel equivalent polarization states of the $ReSe_2$ may be accomplished irreversibly. These tests demonstrate the switchability of polarization in 2L $ReSe_2$ in the presence of an external bias. The surface topography of the $ReSe_2$ nanoflake has not changed after domain writing, according to the AFM images.

Second harmonic generation (SHG) is a non-linear optical method that we utilized to examine the structural changes brought on by the transition from the ferroelectric phase to the paraelectric one. In the investigation of ferroelectric order, the SHG method acts as a sensitive probe for broken inversion symmetry [5, 23]. Using polarization-resolved SHG at room temperature with normal incidence, we investigated the structural symmetry of $ReSe_2$. Figure 5(a) illustrates how the obtained SHG intensity varies with excitation polarization orientation for fixed detection in the horizontal ($I_{//}$) and vertical ($I_{\perp}$) directions using values from a 2L $ReSe_2$ nanoflake. The presence of room-temperature ferroelectricity in 2L $ReSe_2$ is further verified by the non-zero SHG signal. Additionally, we investigated the impact of temperature on the SHG intensity for 2L $ReSe_2$. For comparison, a bulk-form sample has also been evaluated. Figure 5(b) plots the evolution of SHG intensity with increasing temperature. Both the bulk-form and 2L $ReSe_2$ samples exhibit a similar trend: there is an obvious SHG signal below T_c, but the SHG intensity gradually decreases as the temperature increases, and finally, it nearly vanishes at higher temperatures. This strongly implies that for 2L $ReSe_2$, the phase transition from ferroelectric to paraelectric occurs at T_c of around 432 K, which is higher than ambient temperature (see details in Fig. S4 of the ESM). The detailed comparison of the ferroelectric properties of $ReSe_2$ and its sister material, ReS_2, is provided in Fig. S5 of the ESM. Semiconducting $ReSe_2$ with ferroelectricity offers tantalizing opportunities for practical applications due to its high transition temperature.

The Vienna ab initio simulation software (VASP) [33, 34], which incorporates the projected augmented wave (PAW) approach [35] and the Perdew–Burke–Ernzerhof (PBE) [36] exchange-correlation potential function, was used to perform our first-principles DFT calculations. Each unit cell in the monolayer $ReSe_2$ crystal structure has four formula units. The optimized lattice constant of monolayer $ReSe_2$ is 6.65 Å. Monolayer $ReSe_2$ favors a

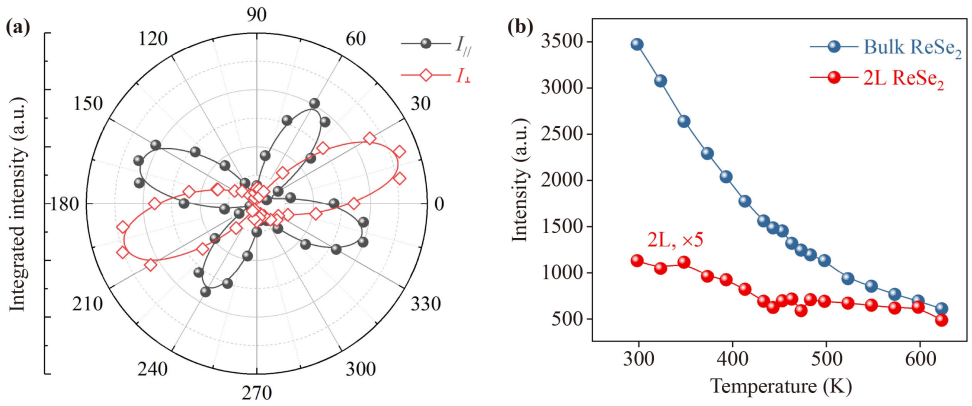

Fig. 5 **(a)** Room-temperature SHG intensity obtained from 2L $ReSe_2$ as a function of the linear excitation polarization angle, along the horizontal ($I_{//}$) and vertical ($I_{\perp}$) directions in laboratory coordinates. **(b)** Temperature dependence of SHG intensity for 2L and bulk-form $ReSe_2$.

1T′ structure with four neighboring Re atoms bonding together to generate diamond-shaped Re chains due to Peierl's distortion. The inversion symmetry in monolayer $ReSe_2$ prohibits the emergence of polarization. For bilayer $ReSe_2$, we move the upper layer along the a and b axes by a sliding distance of (l_a, l_b), respectively, beginning from the AA stacking configuration with xy-plane mirror symmetry. The Berry-phase calculations show that spontaneous polarization occurs in the out-of-plane direction after deviation from AA stacking. The contour of the polarization value is presented in Fig. 6(a). There are two structures with maximum polarization values and opposite polarizing directions, which are marked as states A and A′, respectively. According to calculations, the spontaneous polarization at zero temperature is 0.12 pC/m. The upper layer can be moved by sliding distances of (2.2 Å, 4.6 Å) and (4.4 Å, 2.0 Å), respectively, to obtain the structures of states A and A′, which further reduces the symmetry operation. The vertical polarization originates from an uncompensated charge transfer between two non-equivalent layers in states A and A′. The two structures are energy-degenerate, and state A′ could be created by mirroring state A with regard to the horizontal plane in the center. This results in a reversed vertical polarization, which proves the presence of ferroelectricity. According to the findings, vertical ferroelectricity is strongly correlated with interlayer translation and is switchable upon interlayer sliding. The energy pathway of the ferroelectric transition from state A to A′ is given in Fig. 6(c). Only roughly 4.6 meV per unit cell serves as the energy barrier for this slippage-induced polarization shift. The semiconducting nature and low switching barrier of $ReSe_2$ offer enticing possibilities for functional nanoelectronics applications.

5 Conclusions

In conclusion, by regulating the growth parameters and temperature gradient in the CVT process, semiconducting 1T′-$ReSe_2$ crystals were prepared and then thinned down

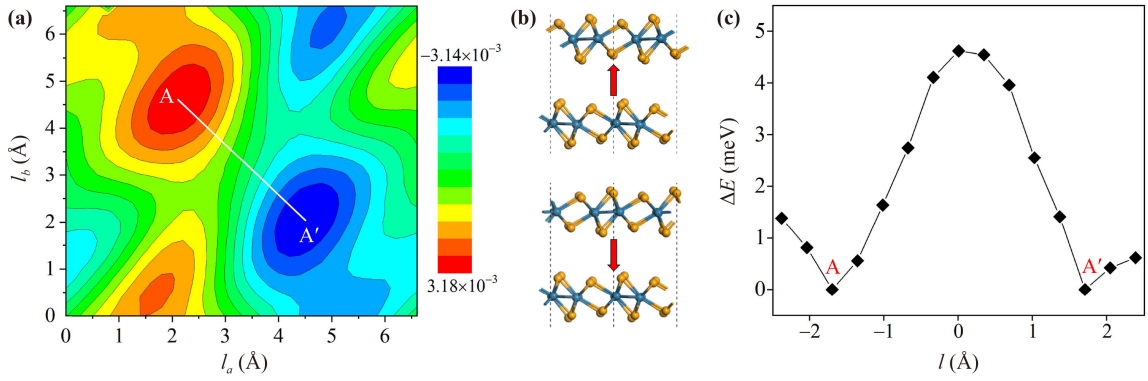

Fig. 6 **(a)** The polarization value contour plot of 2L ReS_2 as a function of sliding distance (l_a, l_b). The states A and A′ are marked. The white line represents the path for ferroelectric transition. **(b)** Side view of the crystal structure of the two energy-degenerate ferroelectric states (A and A′) of 2L $ReSe_2$. The red arrows denote the direction of electric polarization. **(c)** The energy pathway for ferroelectric transition.

to an ultrathin thickness using the standard mechanical exfoliation method. Based on high-resolution TEM characterizations and polarization-dependent Raman scattering measurements, the lack of centrosymmetric and the significant anisotropy resulting from the puckered structure are confirmed. Remarkably, room-temperature robust vertical ferroelectricity was identified in 2L $ReSe_2$ via the experimental investigation of PFM and SHG. Combined with the DFT calculations, we hypothesize that the ferroelectric nature of $ReSe_2$ originates from the uncompensated interlayer charge transfer generated by interlayer sliding. Our findings open up new avenues for the quantum state regulation of 2D materials, laying the theoretical and experimental basis for the design and development of new-principle ferroelectric components.

Electronic supplementary materials The online version contains supplementary material available at https://doi.org/10.1007/s11467-023-1304-4 and https://journal.hep.com.cn/fop/EN/10.1007/s11467-023-1304-4. The data that support the findings of this study are available from the corresponding author upon reasonable request. Figures showing CVT growth, detailed XRD patterns, detailed Raman spectra, ferroelectric transition temperature for 2L $ReSe_2$, and comparison of the ferroelectric properties of $ReSe_2$ and ReS_2.

Declarations The authors declare no competing financial interest.

Acknowledgements This work was financially supported by the National Natural Science Foundation of China (Nos. 12004182 and T2125004), Jiangsu Province Science Foundation (No. BK20200481), and the China Postdoctoral Science Foundation (No. 2021M691587).

References

1. L. W. Martin and A. M. Rappe, Thin-film ferroelectric materials and their applications, *Nat. Rev. Mater.* 2(2), 16087 (2016)
2. M. Wu, 100 years of ferroelectricity, *Nat. Rev. Phys.* 3, 726 (2021)
3. Z. Guan, H. Hu, X. Shen, P. Xiang, N. Zhong, J. Chu, and C. Duan, Recent progress in two-dimensional ferroelectric materials, *Adv. Electron. Mater.* 6(1), 1900818 (2020)
4. C. Wang, L. You, D. Cobden, and J. Wang, Towards two-dimensional van der Waals ferroelectrics, *Nat. Mater.* 22(5), 542 (2023)
5. F. Liu, L. You, K. L. Seyler, X. Li, P. Yu, J. Lin, X. Wang, J. Zhou, H. Wang, H. He, S. T. Pantelides, W. Zhou, P. Sharma, X. Xu, P. M. Ajayan, J. Wang, and Z. Liu, Room-temperature ferroelectricity in $CuInP_2S_6$ ultrathin flakes, *Nat. Commun.* 7(1), 12357 (2016)
6. Y. Li, J. Fu, X. Mao, C. Chen, H. Liu, M. Gong, and H. Zeng, Enhanced bulk photovoltaic effect in two-dimensional ferroelectric $CuInP_2S_6$, *Nat. Commun.* 12(1), 5896 (2021)
7. S. Zhou, L. You, H. Zhou, Y. Pu, Z. Gui, and J. Wang, Van der Waals layered ferroelectric $CuInP_2S_6$: Physical properties and device applications, *Front. Phys.* 16(1), 13301 (2021)
8. C. Cui, W. J. Hu, X. Yan, C. Addiego, W. Gao, Y. Wang, Z. Wang, L. Li, Y. Cheng, P. Li, X. Zhang, H. N. Alshareef, T. Wu, W. Zhu, X. Pan, and L. J. Li, Intercorrelated in-plane and out-of-plane ferroelectricity in ultrathin two-dimensional layered semiconductor In_2Se_3, *Nano Lett.* 18(2), 1253 (2018)
9. S. Wan, Y. Li, W. Li, X. Mao, C. Wang, C. Chen, J. Dong, A. Nie, J. Xiang, Z. Liu, W. Zhu, and H. Zeng, Nonvolatile ferroelectric memory effect in ultrathin α-In_2Se_3, *Adv. Funct. Mater.* 29(20), 1808606 (2019)
10. Y. Cai, J. Yang, F. Wang, S. Li, Y. Wang, X. Zhan, F. Wang, R. Cheng, Z. Wang, and J. He, Ultrasensitive solar-blind ultraviolet detection and optoelectronic neuromorphic computing using α-In_2Se_3 phototransistors, *Front. Phys.* 18(3), 33308 (2023)
11. L. Li and M. Wu, Binary compound bilayer and multilayer with vertical polarizations: Two-dimensional ferroelectrics, multiferroics, and nanogenerators, *ACS Nano* 11(6), 6382 (2017)
12. M. Wu and J. Li, Sliding ferroelectricity in 2D van der Waals materials: Related physics and future opportunities, *Proc. Natl. Acad. Sci. USA* 118(50), e2115703118 (2021)
13. Z. Fei, W. Zhao, T. A. Palomaki, B. Sun, M. K. Miller, Z. Zhao, J. Yan, X. Xu, and D. H. Cobden, Ferroelectric switching of a two-dimensional metal, *Nature* 560(7718), 336 (2018)
14. Q. Yang, M. Wu, and J. Li, Origin of two-dimensional vertical ferroelectricity in WTe_2 bilayer and multilayer, *J. Phys. Chem. Lett.* 9(24), 7160 (2018)
15. P. Sharma, F. X. Xiang, D. F. Shao, D. Zhang, E. Y. Tsymbal, A. R. Hamilton, and J. Seidel, A room-temperature ferroelectric semimetal, *Sci. Adv.* 5(7), eaax5080 (2019)
16. K. Yasuda, X. Wang, K. Watanabe, T. Taniguchi, and P. Jarillo-Herrero, Stacking-engineered ferroelectricity in bilayer boron nitride, *Science* 372(6549), 1458 (2021)
17. M. V. Stern, Y. Waschitz, W. Cao, I. Nevo, K. Watanabe, T. Taniguchi, E. Sela, M. Urbakh, O. Hod, and M. B. Shalom, Interfacial ferroelectricity by van der Waals sliding, *Science* 372(6549), 1462 (2021)
18. C. R. Woods, P. Ares, H. Nevison-Andrews, M. J. Holwill, R. Fabregas, F. Guinea, A. K. Geim, K. S. Novoselov, N. R. Walet, and L. Fumagalli, Charge-polarized interfacial superlattices in marginally twisted hexagonal boron nitride, *Nat. Commun.* 12(1), 347 (2021)
19. Y. Wang, S. Jiang, J. Xiao, X. Cai, D. Zhang, P. Wang, G. Ma, Y. Han, J. Huang, K. Watanabe, T. Taniguchi, Y. Guo, L. Wang, A. S. Mayorov, and G. Yu, Ferroelectricity in *h*BN intercalated double-layer graphene, *Front. Phys.* 17(4), 43504 (2022)
20. H. Hu, H. Wang, Y. Sun, J. Li, J. Wei, D. Xie, and H. Zhu, Out-of-plane and in-plane ferroelectricity of atom-thick two-dimensional InSe, *Nanotechnology* 32(38), 385202 (2021)
21. F. Sui, M. Jin, Y. Zhang, R. Qi, Y. N. Wu, R. Huang, F. Yue, and J. Chu, Sliding ferroelectricity in van der Waals layered γ-InSe semiconductor, *Nat. Commun.*

14(1), 36 (2023)
22. L. Rogée, L. Wang, Y. Zhang, S. Cai, P. Wang, M. Chhowalla, W. Ji, and S. P. Lau, Ferroelectricity in untwisted heterobilayers of transition metal dichalcogenides, *Science* 376(6596), 973 (2022)
23. Y. Wan, T. Hu, X. Mao, J. Fu, K. Yuan, Y. Song, X. Gan, X. Xu, M. Xue, X. Cheng, C. Huang, J. Yang, L. Dai, H. Zeng, and E. Kan, Room-temperature ferroelectricity in 1T′-ReS_2 multilayers, *Phys. Rev. Lett.* 128(6), 067601 (2022)
24. L. P. Miao, N. Ding, N. Wang, C. Shi, H. Y. Ye, L. Li, Y. F. Yao, S. Dong, and Y. Zhang, Direct observation of geometric and sliding ferroelectricity in an amphidynamic crystal, *Nat. Mater.* 21(10), 1158 (2022)
25. B. Jariwala, D. Voiry, A. Jindal, B. A. Chalke, R. Bapat, A. Thamizhavel, M. Chhowalla, M. Deshmukh, and A. Bhattacharya, Synthesis and characterization of ReS_2 and $ReSe_2$ layered chalcogenide single crystals, *Chem. Mater.* 28(10), 3352 (2016)
26. J. Ran, L. Chen, D. Wang, A. Talebian-Kiakalaieh, Y. Jiao, M. Adel Hamza, Y. Qu, L. Jing, K. Davey, and S. Z. Qiao, Atomic-level regulated two-dimensional $ReSe_2$: A universal platform boosting photocatalysis, *Adv. Mater.* 2023, 2210164 (2023)
27. L. Xing, X. Yan, J. Zheng, G. Xu, Z. Lu, L. Liu, J. Wang, P. Wang, X. Pan, and L. Jiao, Highly crystalline $ReSe_2$ atomic layers synthesized by chemical vapor transport, *InfoMat* 1(4), 552 (2019)
28. A. S. Rosyadi, A. H. Y. Chan, J. X. Li, C. H. Liu, and C. H. Ho, Formation of van der Waals stacked *p*–*n* homojunction optoelectronic device of multilayered $ReSe_2$ by Cr doping, *Adv. Opt. Mater.* 10(13), 2200392 (2022)
29. M. Hafeez, L. Gan, H. Li, Y. Ma, and T. Zhai, Chemical vapor deposition synthesis of ultrathin hexagonal $ReSe_2$ flakes for anisotropic Raman property and optoelectronic application, *Adv. Mater.* 28(37), 8296 (2016)
30. P. Blake, E. W. Hill, A. H. Castro Neto, K. S. Novoselov, D. Jiang, R. Yang, T. J. Booth, and A. K. Geim, Making graphene visible, *Appl. Phys. Lett.* 91(6), 063124 (2007)
31. H. Li, G. Lu, Z. Yin, Q. He, H. Li, Q. Zhang, and H. Zhang, Optical identification of single-and few-layer MoS_2 sheets, *Small* 8(5), 682 (2012)
32. Y. Y. Wang, J. D. Zhou, J. Jiang, T. T. Yin, Z. X. Yin, Z. Liu, and Z. X. Shen, In-plane optical anisotropy in ReS_2 flakes determined by angle-resolved polarized optical contrast spectroscopy, *Nanoscale* 11(42), 20199 (2019)
33. G. Kresse and J. Hafner, *Ab initio* molecular dynamics for open-shell transition metals, *Phys. Rev. B* 48(17), 13115 (1993)
34. G. Kresse and J. Furthmüller, Efficiency of *ab-initio* total energy calculations for metals and semiconductors using a plane-wave basis set, *Comput. Mater. Sci.* 6(1), 15 (1996)
35. G. Kresse and D. Joubert, From ultrasoft pseudopotentials to the projector augmented-wave method, *Phys. Rev. B* 59(3), 1758 (1999)
36. J. P. Perdew, K. Burke, and M. Ernzerhof, Generalized gradient approximation made simple, *Phys. Rev. Lett.* 77(18), 3865 (1996)